Topological phenomena in classical optical networks

T. Shi[a,1], H. J. Kimble[b,1], and J. I. Cirac[a]

[a]Max-Planck-Institut für Quantenoptik, 85748 Garching, Germany; and [b]Norman Bridge Laboratory of Physics, California Institute of Technology, Pasadena, CA 91125

Contributed by H. J. Kimble, September 13, 2017 (sent for review June 5, 2017; reviewed by Mohammad Hafezi and Mikael C. Rechtsman)

We propose a scheme to realize a topological insulator with optical-passive elements and analyze the effects of Kerr nonlinearities in its topological behavior. In the linear regime, our design gives rise to an optical spectrum with topological features and where the bandwidths and bandgaps are dramatically broadened. The resulting edge modes cover a very wide frequency range. We relate this behavior to the fact that the effective Hamiltonian describing the system's amplitudes is long range. We also develop a method to analyze the scheme in the presence of a Kerr medium. We assess robustness and stability of the topological features and predict the presence of chiral squeezed fluctuations at the edges in some parameter regimes.

topology | nonlinear | network | optical

The discovery of topological insulators (TIs), as well as quantum spin Hall (QSH) insulators (1–9), has opened up a wide range of scientific and technological questions. Their spectra feature a set of bands, connected by chiral edge modes that reflect the topological nature of the material. These modes are robust against perturbations whose energy does not exceed the corresponding bandgap and that do not break the time-reversal (TR) symmetry (10, 11). Electronic interactions give rise to a wide range of phenomena. Although the edge modes persist, their properties are qualitatively modified (12). In addition, they can give rise to other exotic phenomena, like the fractionalization of charges, or the appearance of excitations with fractional statistics (13, 14).

Recent proposals to generate TIs and QSH insulators with light have also attracted a lot of attention (2, 15–27, 28). In fact, the first experimental observations (15, 16) of topological features in optical systems have been recently reported, and several schemes exhibiting intriguing features have been proposed (17–25). There exist different setups where one can realize the optical analog of QSH insulators and observe similar features. In the context of coupled resonator arrays, one can use either differential optical paths in waveguides (26) or an optical active element (27). Despite their success, in the first case it would be desirable to enlarge the bandgaps in the spectrum, which is limited by the small coupling of the local modes in the (high-finesse) resonators (26), to gain robustness. To enlarge the bandwidth and bandgaps, recently, several proposals in the Floquet systems (29), microwave networks (30), and strongly coupled spoof-plasmon systems (31) have been studied. In the second one, photon absorption in the active media also limits the operationality of the scheme. In other schemes, like the one based on bianisotropic metacrystals (28), the realization of long-lived edge modes in a broader frequency range is challenged by the weak bianisotropy in metamaterials (32, 33). To enhance the bianisotropy, an alternative realization has been proposed for metallodielectric photonic crystals in the microwave regime (34). The effects of interactions, including the stability of edge modes, edge solitons, and the quantum dynamics, in those optical models have been also investigated recently (24, 35–42).

In this work we propose and analyze a scheme to realize the optical version of the QSH insulator and investigate the effects produced by Kerr nonlinearities. Our scheme uses beam splitters and birefringent materials that are optically passive and thus circumvent the problem of photon absorption. Our scheme features several distinct phenomena compared with some of the previous proposals.

In the linear regime, the Hamiltonian description of our setup features long-range hopping, which leads to a dramatic increase of the spectral bands and bandgaps. This results in a more robust behavior of the edge modes against perturbations. We analyze quantitatively the robustness of our scheme against losses and compare it to other models not displaying long-range Hamiltonian descriptions, as well as to recent experiments (15).

In the nonlinear regime, we obtain the following results: (*i*) In a closed network, an arbitrarily small Kerr interaction induces instability, a phenomenon we explain in terms of a simple model. (*ii*) Opening the network and driving it in the appropriate regime stabilizes the system. By tuning the frequency of the driven light, stable bulk and edge modes are both generated. (*iii*) The small excitations around the edge modes are themselves chiral and thus protected. (*iv*) The edge modes, apart from being chiral, are squeezed.

In this paper we also introduce theoretical frameworks based on the S-matrix approach to describe our model both for the linear and for the nonlinear regimes. The reason why standard approaches do not apply in the linear regime is that the energy spectrum spreads over the whole free spectral range (FSR), so that the energy bands in two adjacent ranges connect to each other. Thus, one cannot use an effective Hamiltonian description in each FSR. Furthermore, since the energy spectrum is not lower bounded, the nonlinear behavior is very different from that of lower-bounded Hamiltonians. The analysis of such behavior cannot be carried out with standard Bogoliugov techniques, but requires a sophisticated method based on a nonlinear S-matrix formalism.

Model Setup

In this section, we construct (non)linear classical optical networks that exhibit nontrivial phenomena. The light propagation

Significance

We introduce a unique scheme to investigate topological behavior, using optical-passive elements and Kerr nonlinearities. Compared with previous proposals, the topological band gaps are dramatically broadened, leading to very robust edge modes. Our setup displays intriguing phenomena in the nonlinear regime, including instabilities and the production of squeezed light in the edge modes. This proposal promises unique avenues for engineering phases of light with topological character.

Author contributions: T.S., H.J.K., and J.I.C. designed research; T.S., H.J.K., and J.I.C. performed research; T.S. contributed new reagents/analytic tools; T.S. analyzed data; and T.S., H.J.K., and J.I.C. wrote the paper.

Reviewers: M.H., University of Maryland; and M.C.R., Pennsylvania State University.

The authors declare no conflict of interest.

[1]To whom correspondence may be addressed. Email: tshi@mpq.mpg.de or hjkimble@caltech.edu.

This article contains supporting information online at www.pnas.org/lookup/suppl/doi:10.1073/pnas.1708944114/-/DCSupplemental.

in the nodes and (non)linear fibers is investigated in *Nodes* and *Light Propagation in Fibers*, respectively. In *Full Networks*, we analyze the boundary conditions for the closed and open networks in the torus, cylinder, and open plane.

We consider a toy model, i.e., a network of size $N_x \times N_y$ with optically passive elements. As shown in Fig. 1 *A* and *B*, at each node of a square lattice, two beamsplitters and two perfect mirrors form a "bad cavity" to change the propagation direction of incoming light in the optical fibers with length L. The fibers 1 and 4 are connected to the beamsplitter A, and the fibers 2 and 3 are connected to the beamsplitter B.

Since the polarizations of light are always orthogonal to the propagation direction, the directions of vertical polarization V in the horizontal and vertical fibers are different. As shown in Fig. 1*B*, the directions of horizontal polarization H are chosen to be pointing out of the 2D plane, while the directions of vertical polarization V are pointing up and right in the horizontal and vertical fibers, respectively.

Nodes. In this subsection we study the light propagation in the node, where the relation of input and output amplitudes $\Psi_a = (a_r, a_u, a_l, a_d)^T$ and $\Psi_b = (b_r, b_u, b_l, b_d)^T$ (Fig. 1*B*) is established by the scattering matrix (S matrix) of the node. Here, the two-component amplitudes $a_{r,u,l,d}$ and $b_{r,u,l,d}$ are defined in the linear polarization basis (H, V). As shown in Fig. 1*B*, in the inner cavity, the input and output amplitudes of the beamsplitter A are $c_{u,l}$ and $c_{r,d}$, and the elements C and D are perfectly reflecting mirrors.

The relation

$$S_{\rm bs}^{(A)} \begin{pmatrix} \sigma_z a_r \\ c_u \\ c_l \\ a_d \end{pmatrix} = \begin{pmatrix} c_r \\ b_u \\ \sigma_z b_l \\ c_d \end{pmatrix}; S_{\rm bs}^{(B)} \begin{pmatrix} c_d \\ \sigma_z a_u \\ a_l \\ c_r \end{pmatrix} = \begin{pmatrix} b_r \\ c_l \\ c_u \\ \sigma_z b_d \end{pmatrix}, \quad [1]$$

between amplitudes $a_{r,u,l,d}$, $b_{r,u,l,d}$, and $c_{r,u,l,d}$ is determined by the S-matrix $S_{\rm bs}^{(A)} = S_{\rm bs}^{(B)} \equiv S_{\rm bs}$,

$$S_{\rm bs} = \begin{pmatrix} t_{\rm bs} & ir_{\rm bs}\sigma_z & 0 & 0 \\ ir_{\rm bs}\sigma_z & t_{\rm bs} & 0 & 0 \\ 0 & 0 & t_{\rm bs} & ir_{\rm bs}\sigma_z \\ 0 & 0 & ir_{\rm bs}\sigma_z & t_{\rm bs} \end{pmatrix} \quad [2]$$

of beamsplitters A and B, where the real reflection and transmission coefficients are $r_{\rm bs}$ and $t_{\rm bs} = \sqrt{1 - r_{\rm bs}^2}$. In Eq. **1**, we have assumed that the size of the node is much smaller than the wavelength of light such that the free propagation phase in the node can be neglected. In principle, for a node cavity of small dimensions compared with the optical wavelength, the diffraction effect should be considered and a full finite-difference time-domain method might be required. In practice, one should consider designing coupling directly the fiber to the cavities and a design such that losses are negligible. Under such conditions, the node will be characterized by a set of parameters, i.e., the reflection and transmission coefficients, that could be adjusted to match the toy model considered here. We expect that our toy model can capture the main physics in the system. A similar treatment was used in ref. 27.

Due to the Fresnel reflection rule, for the incoming vertical polarized light from the fiber 1 (3), the reflecting light in the fiber 4 (2) changes the sign. The sign change for the vertical polarization is described by the Pauli matrix σ_z in Eq. **2**. To cancel this Fresnel effect, two birefringent elements E and F in close proximity to the beamsplitters (A, B) in the fibers 1 and 2 have been introduced and are described by the Jones matrix σ_z in Eq. **1**.

Eliminating the inner-cavity fields $c_{r,u,l,d}$, we derive the scattering equation $S_{\rm node}\Psi_a = \Psi_b$ at the node, where the S-matrix

$$S_{\rm node} = \begin{pmatrix} 0 & ir_{\rm node} & 0 & t_{\rm node} \\ ir_{\rm node} & 0 & t_{\rm node} & 0 \\ 0 & t_{\rm node} & 0 & ir_{\rm node} \\ t_{\rm node} & 0 & ir_{\rm node} & 0 \end{pmatrix} \quad [3]$$

relates the input and the output amplitudes Ψ_a and Ψ_b. At the node, the effective reflection and transmission coefficients are $r_{\rm node} = 2r_{\rm bs}/(1 + r_{\rm bs}^2)$ and $t_{\rm node} = t_{\rm bs}^2/(1 + r_{\rm bs}^2)$, respectively. In our scheme, we choose $r_{\rm bs} = \sqrt{2} - 1$, such that $r_{\rm node} = t_{\rm node} = 1/\sqrt{2}$ maximizes the topological bandwidth and bandgap defined later on.

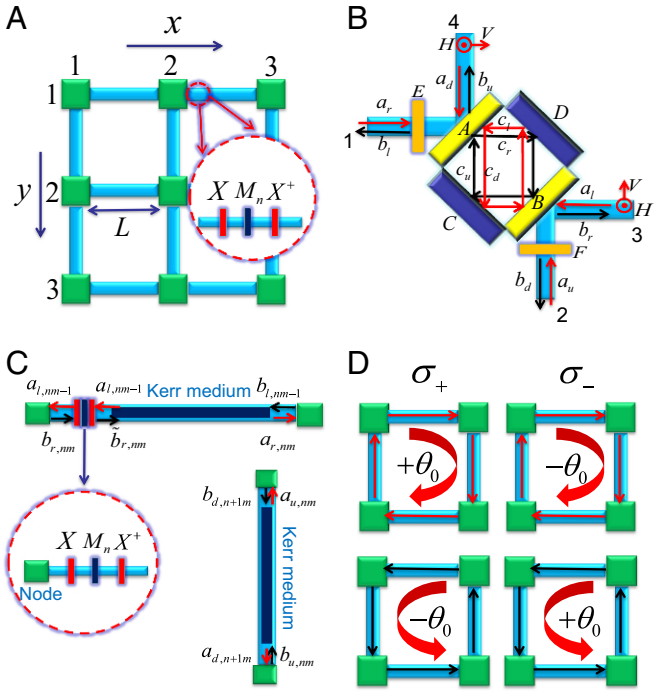

Fig. 1. Scheme of our optical network. (*A*) The planar network. (*B*) A node connects horizontal and vertical links. Here, $a_{r,u,l,d}$ and $b_{r,u,l,d}$ denote the input and output amplitudes, and $c_{r,u,l,d}$ denotes the amplitudes in the cavity. The horizontal and vertical polarizations (*H*,*V*) in fibers are shown by the red circles and arrows. (*C*) The horizontal and vertical links with the Kerr medium and birefringent elements, where the Kerr medium is put on the right-hand side of three birefringent elements in the horizontal link, where the birefringent elements are assumed to have no Kerr nonlinearity ($\chi = 0$). From left to right, the three birefringent elements are described by the Jones matrices $X = e^{i\pi\sigma x/4}$, $M_n = e^{in\theta_0\sigma z}$, and $X^\dagger$ in the linear polarization basis (*H*, *V*). (*D*) The σ_+ polarized light acquires the phase θ_0 ($-\theta_0$) by propagating (anti)clockwisely in each plaquette, while the σ_- polarized light acquires the phase $-\theta_0$ (θ_0) by propagating (anti)clockwisely in each plaquette.

Light Propagation in Fibers. In this subsection, we use a wave equation to study the light propagation in the nonlinear fiber connecting two adjacent nodes, where the birefringent elements are introduced to induce the artificial gauge field for the light. By solving the wave equation, we obtain the input–output relation of the amplitudes at adjacent nodes.

Fig. 1*C* shows that in each horizontal fiber, three birefringent elements described by the Jones matrices $X = e^{i\pi\sigma_x/4}$, $M_n = e^{in\theta_0\sigma_z}$, and $X^\dagger$ are placed close to the node on the left side of the horizontal fiber, where $\sigma_{x,y,z}$ are Pauli matrices in the polarization basis (H, V). The element with the row-dependent Jones matrix M_n generates the opposite phase shifts $\pm n\theta_0$ for the H- and V-polarized light, and the element with the Jones matrix X induces the phase shifts $\pm\pi/4$ for the linear polarized light $(H \pm V)/\sqrt{2}$. The birefringent elements cause the light to acquire a phase matrix $\theta_0\sigma_y$ by propagating around

each plaquette. Eventually, circular polarizations $(H \pm iV)/\sqrt{2}$ ($\sigma_\pm$) experience oppositely directed "magnetic" fields with fluxes $\pm\theta_0$ (Fig. 1*D*), which induces a nontrivial Z_2 topology in this TR-invariant system.

The interaction of light in the fiber, induced by a Kerr nonlinearity (Fig. 1*C*), leads to the additional phase proportional to the light intensity. We set to zero the cross-phase modulation between orthogonal circular polarizations in the Kerr nonlinearity, as discussed in ref. 43, chap. 6 and ref. 44, chap. 4. As a result, the two polarizations are decoupled, and we are able to treat the $\sigma_\pm$ polarizations independently, as long as these polarizations are separately excited by the external input (i.e., only σ_+ or σ_- polarization circulating in the fiber links).

In the Kerr medium of the fiber connecting nodes (n, m) and $(n, m-1)$, the right- and left-moving fields $\phi_{r(l),nm}$ (denoting the left or right polarized light) obey the motion equations (45–47) (we use the matrix convention (n, m) to label the sites, where n is the row index and m is the column index; we note that the matrix convention is different from the coordinate convention (x, y) that labels the row and column by y and x, respectively)

$$i\partial_t\phi_{r,nm}(x,t) + i\partial_x\phi_{r,nm}(x,t) = \chi[|\phi_{r,nm}(x,t)|^2 + 2|\phi_{l,nm-1}(x,t)|^2]\phi_{r,nm}(x,t), \quad [4]$$

and

$$i\partial_t\phi_{l,nm-1}(x,t) - i\partial_x\phi_{l,nm-1}(x,t) = \chi[|\phi_{l,nm-1}(x,t)|^2 + 2|\phi_{r,nm}(x,t)|^2]\phi_{l,nm-1}(x,t), \quad [5]$$

where x is the distance along the fiber and χ describes the self-focusing Kerr interaction (43, 48). In *Light Propagation in Single-Segment Nonlinear Fiber* and Figs. S1 and S2, we give the solution of the motion Eqs. **4** and **5** in detail.

The wave Eq. **4** has the solution

$$\phi^{(0)}_{r,nm}(x,t) = a_{r,nm}\,e^{ik_r(x-L)}\,e^{-i\omega t},$$
$$\phi^{(0)}_{l,nm-1}(x,t) = \tilde{a}_{l,nm-1}\,e^{-ik_l x}\,e^{-i\omega t}, \quad [6]$$

where, as shown in Fig. 1*C*, $a_{r,nm}$ is the amplitude of the right-moving input field to the node (n, m), and $\tilde{a}_{l,nm-1}$ is the amplitude of the left-moving input field to the birefringent elements. The wave vectors

$$k_r = \omega - \chi[|a_{r,nm}|^2 + 2|\tilde{a}_{l,nm-1}|^2],$$
$$k_l = \omega - \chi[|\tilde{a}_{l,nm-1}|^2 + 2|a_{r,nm}|^2] \quad [7]$$

of the right- and left-moving fields are determined by the intensities of the fields and the frequency ω of light in the fiber.

The solution **6** results in the relation

$$e^{-in\sigma\theta_0}\,b_{r,nm} = \tilde{b}_{r,nm} = e^{-ik_rL}\,a_{r,nm},$$
$$e^{in\sigma\theta_0}\,b_{l,nm-1} = e^{-ik_lL}e^{in\sigma\theta_0}\,\tilde{a}_{l,nm-1} = e^{-ik_lL}\,a_{l,nm-1}, \quad [8]$$

where $b_{r,nm}$ is the amplitude of the right-moving output field out of the node $(n, m-1)$, $\tilde{b}_{r,nm}$ is the amplitude of the right-moving field on the right-hand side of the birefringent elements, $b_{l,nm-1}$ is the amplitude of the left-moving output field out of the node (n, m), $a_{l,nm-1}$ is the amplitude of the left-moving input field to the node $(n, m-1)$, and $\sigma = \pm 1$ for the two orthogonal circular polarizations.

The same analysis is applied to the light propagation in the vertical fiber connecting the nodes (n, m) and $(n+1, m)$. The steady-state solution of Eq. **5** results in the relation

$$b_{u,nm} = e^{-ik_uL}a_{u,nm},\ b_{d,n+1m} = e^{-ik_dL}a_{d,n+1m}, \quad [9]$$

for the amplitudes of input fields $a_{u,nm}, a_{d,n+1m}$ and output fields $b_{u,nm}, b_{d,n+1m}$ (as shown in Fig. 1*C*), where the wave vectors are

$$k_u = \omega - \chi[|a_{u,nm}|^2 + 2|a_{d,n+1m}|^2],$$
$$k_d = \omega - \chi[|a_{d,n+1m}|^2 + 2|a_{u,nm}|^2]. \quad [10]$$

The S-matrix **3** of the node and the relations **8** and **9** determine the light distribution in the bulk of the network.

Full Networks. In this subsection, different boundary conditions are studied for the closed networks in the torus, cylinder, and open plane. To generate the nontrivial topological states in the network, we drive the open network by external light through the boundary.

To realize the cylindrical and planar geometries, perfect mirrors are placed along the boundaries to form the closed network, where the distance between the boundary mirror and the boundary node is $L/2$ (Fig. 2 *A* and *B*). The boundary conditions are

$$a_{r,nN_x+1} = a_{r,n1},\ a_{l,n0} = a_{l,nN_x},$$
$$a_{u,0m} = a_{u,N_ym},\ a_{d,N_y+1m} = a_{d,1m} \quad [11]$$

for the network in the torus,

$$a_{r,nN_x+1} = a_{r,n1},\ a_{l,n0} = a_{l,nN_x},$$
$$a_{u,0m} = a_{d,1m},\ a_{d,N_y+1m} = a_{u,N_ym} \quad [12]$$

for the closed cylindrical network with the periodic boundary condition along the x direction, and

$$a_{r,nN_x+1} = a_{l,nN_x},\ a_{l,n0} = a_{r,n1},$$
$$a_{u,0m} = a_{d,1m},\ a_{d,N_y+1m} = a_{u,N_ym} \quad [13]$$

for the planar network with boundary perfect mirrors.

Through the partially transmissive mirrors at the boundary of the open networks, nontrivial topological states can be generated by the external optical driving field. For the open cylindrical network, we drive the network through the top boundary mirrors with the reflection (transmission) coefficient $r_{\rm BM}$ ($t_{\rm BM}$), as shown in Fig. 2*C*, where the driving light of frequency $\omega_{\rm d}$ has the amplitude $A^{(0)}_{{\rm in},m}$. The corresponding boundary condition

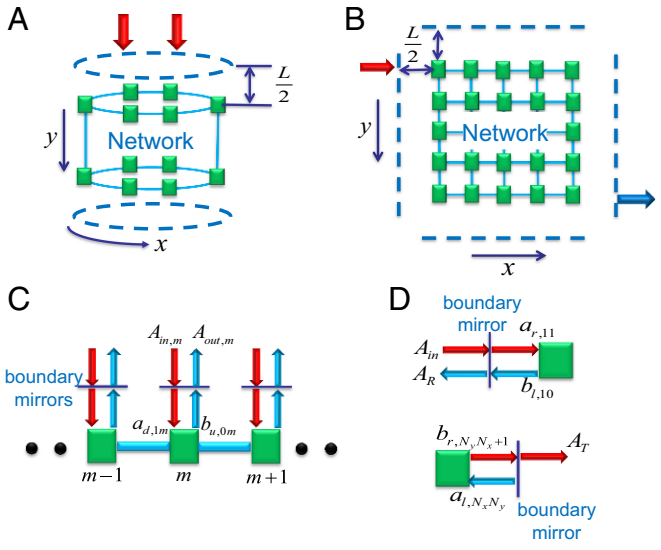

Fig. 2. Scheme for the boundary mirrors in the cylindrical and planar networks. (*A* and *B*) Perfect and partially transmissive mirrors are put along the boundaries of the cylindrical (*A*) and planar (*B*) networks. Here, the partially transmissive mirrors are placed along the top boundary in the cylindrical network and at the top left and bottom right corners in the planar network. The driving light (red arrows) is applied to generate the excitations and the transmitted light (blue arrow). (*C*) Driven cylindrical network through each of the partially transmissive mirrors on the top boundary. (*D*) Light reflection and transmission through the boundary mirrors next to the nodes (1, 1) and (N_y, N_x) in the planar network (i.e., nodes in the top left and bottom right corners of the planar network).

$$S_{\rm BM}\begin{pmatrix} A^{(0)}_{{\rm in},m} \\ b_{u,0m}\,e^{i\omega_{\rm d}L/2}\end{pmatrix}=\begin{pmatrix} a_{d,1m}\,e^{-i\omega_{\rm d}L/2} \\ A^{(0)}_{{\rm out},m}\end{pmatrix} \quad [14]$$

is determined by the S-matrix

$$S_{\rm BM}=\begin{pmatrix} t_{\rm BM} & ir_{\rm BM} \\ ir_{\rm BM} & t_{\rm BM}\end{pmatrix} \quad [15]$$

of the transmissive mirrors, where $A^{(0)}_{{\rm out},m}$ is the amplitude of the output field above the boundary mirror (Fig. 2*C*), and $a_{d,1m}$ and $b_{u,0m}$ are the amplitudes of the down-moving input field and the up-moving output field at the top of the cylinder [i.e., the boundary node $(1,m)$].

For the open planar network, we drive the network through the partially transmissive mirror next to the node $(1,1)$ with light of frequency $\omega_{\rm d}$ and detect the transmission to the node (N_x,N_y), as shown in Fig. 2*D*. The boundary condition is

$$S_{\rm BM}\begin{pmatrix} A^{(0)}_{\rm in} \\ b_{l,10}\,e^{i\omega_{\rm d}L/2}\end{pmatrix}=\begin{pmatrix} a_{r,11}\,e^{-i\omega_{\rm d}L/2} \\ A_{\rm R}\end{pmatrix},$$
$$S_{\rm BM}\begin{pmatrix} b_{r,N_yN_x+1}\,e^{i\omega_{\rm d}L/2} \\ 0\end{pmatrix}=\begin{pmatrix} A_{\rm T} \\ a_{l,N_yN_x}\,e^{-i\omega_{\rm d}L/2}\end{pmatrix}, \quad [16]$$

where $A^{(0)}_{\rm in}$ denotes the input amplitude to the network, and $A_{\rm R}$ ($A_{\rm T}$) is the reflection (transmission) amplitude. The amplitudes of right-moving input and left-moving output fields at the node $(1,1)$ are $a_{r,11}$ and $b_{l,10}$, while the amplitudes of left-moving input and right-moving output fields at the node (N_x,N_y) are a_{l,N_yN_x} and b_{r,N_yN_x+1}.

Using the S-matrix **3** at the node, the relations **8** and **9**, and the boundary conditions **14** and **16**, we can establish the scattering equations for the entire network in the different geometries. The details are shown in *Scattering Equations on Different Geometries*.

Linear Regime

In this section, we use the scattering equation to study the topological phenomena in the linear network without the Kerr medium. In *Topological Band Structures in Closed Networks*, we study the photonic spectra $\mathcal{E}$ by solving the scattering equation for the closed networks in the torus, cylinder, and open plane. We find that the edge states appear in the bandgaps covering a very wide frequency range. In *Probe Edge and Bulk Modes in Open Networks*, we show that the edge and bulk modes can be generated by the external driving light and detected by the spectroscopic analysis of the transmitted light. The robustness of the edge modes against losses and imperfections is analyzed in *Robustness of the Edge Modes in Open Networks*.

The photonic spectra $\mathcal{E}$ of the closed linear networks in different geometries exhibit nontrivial topological phenomena, which are described by the scattering equation. For the bulk degrees of freedoms, the scattering equation

$$S_0\begin{pmatrix} a_{r,nm} \\ a_{u,nm} \\ a_{l,nm} \\ a_{d,nm}\end{pmatrix}=e^{-i\mathcal{E}L}\begin{pmatrix} a_{r,nm+1} \\ a_{u,n-1m} \\ a_{l,nm-1} \\ a_{d,n+1m}\end{pmatrix} \quad [17]$$

follows from Eqs. **8** and **9**, where the free S-matrix

$$S_0=\frac{1}{\sqrt{2}}\begin{pmatrix} 0 & ie^{-in\sigma\theta_0} & 0 & e^{-in\sigma\theta_0} \\ i & 0 & 1 & 0 \\ 0 & e^{in\sigma\theta_0} & 0 & ie^{in\sigma\theta_0} \\ 1 & 0 & i & 0\end{pmatrix} \quad [18]$$

connects the right-, up-, left-, and down-moving input fields $a_{r,u,l,d,nm}$ at the node (n,m) with the input amplitudes $a_{r,nm+1}$, $a_{u,n-1,m}$, $a_{l,nm-1}$, and $a_{d,n+1m}$ at the four nearest-neighbor nodes. We note that the eigenstates of S_0 have well-defined polarization σ_+ or σ_-.

Topological Band Structures in Closed Networks. Incorporating the boundary conditions **11** and **12** to the scattering Eq. **17**, we determine the eigenstates and the corresponding spectrum. Due to the translational symmetry, the eigenstate

$$a_{(r,u,l,d),nm}=\frac{1}{\sqrt{N_x}}\,a_{(r,u,l,d),n}\,e^{ik_xm} \quad [19]$$

has well-defined quasi-momenta $k_x=-\pi+2\pi n/N_x$, where $n=0,1,2,...,N_x-1$.

Fig. 3 *A* and *B* shows the spectra of the networks in the torus and cylinder in the FSR $\mathcal{E}\in\omega_c+(-\pi/L,\pi/L]$ around a large central frequency $\omega_c=2\pi N_c/L$, where N_c is a positive integer, and $\theta_0=\pi/2$.

As shown in Fig. 3*A*, in the torus the photonic bands spread over the whole FSR $2\pi/L$ and display large bandgaps. For instance, for $L=50$ μm (15), the FSR is $\sim 1THz$. In contrast to the standard narrow-band schemes (26, 27), the wide-band spectrum results from the large hopping strength (comparable with $2\pi/L$) between nodes beyond nearest neighbors in the bad cavity regime, $R_{\rm bs}=|r_{\rm bs}|^2\sim 0.17$. In each FSR, this long-range hopping behavior is characterized by the spatially nonlocal Hamiltonian $H_{\rm eff}=i\,\ln S_0/L$ rather than the Hofstadter (tight binding) model (49). Here, we emphasize that even though the S matrix contains only the nearest-neighbor couplings, the effective Hamiltonian could show long-range hopping behavior between cavity modes since it is determined by the logarithm of the S matrix. One can introduce the creation (annihilation) operators $C_{k,\alpha}$ of the eigenmodes in the band α to express the effective Hamiltonian as $H_{\rm eff}=\sum_k \varepsilon_{k,\alpha}\,C^\dagger_{k,\alpha}C_{k,\alpha}$, where $\varepsilon_{k,\alpha}$ denotes the dispersion relation in the band α.

As a consequence of time-reversal symmetry [as in the case of Z_2-protected topological insulators (10)], helical edge modes arise at the broad topological bandgaps. In Fig. 3*B*, for the cylindrical geometry, the spectrum displays four edge modes between

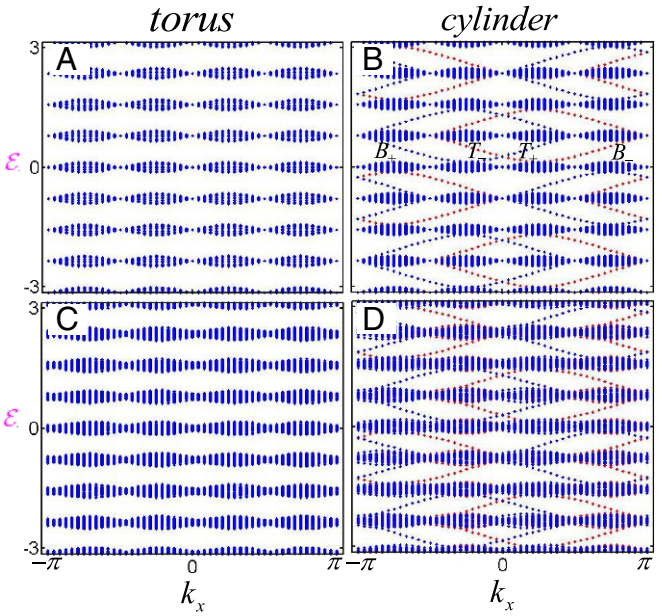

Fig. 3. The energy spectra in the torus and cylinder, where $\theta_0=\pi/2$, the network size is 48 × 48, and L is taken as a unit. Here, we use $T_\pm$ and $B_\pm$ to denote the $\sigma_\pm$ polarizations on the top and bottom boundaries, respectively. (*A* and *B*) The energy spectrum $\mathcal{E}$ in the torus (*A*) and cylinder (*B*) without phase randomness and losses of linear elements, where *B* and *T* denote the bottom and top boundaries, respectively. (*C* and *D*) The real part of the energy spectrum in the torus (*C*) and cylinder (*D*) with phase randomness and nonzero losses of linear elements.

the bandgaps, where the chiralities of two edge modes on each boundary are locked to the $\sigma_\pm$ polarizations. We focus on the right polarized mode. The Chern number associated to the right polarized mode in each subband can be properly defined. The lowest and highest subbands in each FSR have Chern number 1. From the second to the eighth subbands, the Chern number changes alternatively between two values, ± 2. As a result, the right polarized edge mode localized at the top boundary of the cylinder changes its chirality alternatively in different midgaps. This band structure is similar to that found in Floquet systems (50).

These helical edge modes are robust to local perturbations that do not break the time-reversal symmetry, as long as the bandgap remains open. As we shall see in *Robustness of the Edge Modes in Open Networks*, the effects of randomness and losses are strongly suppressed due to the broadness of the spectrum as a consequence of the low finesse of the cavities. Fig. 3 *C* and *D* shows that for random phase fluctuations $\delta_p \in [-0.2, 0.2]$ around $\theta_0 = \pi/2$ and a 10% optical loss in each element, the bandgaps in the energy spectrum Re$\mathcal{E}$ are still open in the torus, and the helical edge modes survive in the cylinder with lifetime $\tau = 1/\mathrm{Im}\mathcal{E} \sim 13L$. The losses are described by the nonunitary S matrix of the optical element.

Probe Edge and Bulk Modes in Open Networks. To generate and detect the edge and bulk modes, we consider the open networks in the torus and cylinder driven by an external light, as shown in Fig. 2 *C* and *D*.

For the cylindrical network (Fig. 2*A*), the input light

$$A^{(0)}_{\mathrm{in},m}(t) = \frac{1}{\sqrt{N_x}} A^{(0)}_{\mathrm{in}}\, e^{ik_x m - i\omega_\mathrm{d} t} \qquad [20]$$

with amplitude $A^{(0)}_{\mathrm{in}}$ and frequency ω_d is applied through the transmissive top-boundary mirror. Due to the translational symmetry in the driven network, the steady-state solution has the form **19**. The boundary condition **14** and the scattering Eq. **17** result in

$$S_{\mathrm{BM}} \begin{pmatrix} A^{(0)}_{\mathrm{in}} \\ b_{u,0}\, e^{i\omega_\mathrm{d} L/2} \end{pmatrix} = \begin{pmatrix} a_{d,1}\, e^{-i\omega_\mathrm{d} L/2} \\ A^{(0)}_{\mathrm{out}} \end{pmatrix}, \qquad [21]$$

and

$$R_{\mathrm{BM}} S_0(k_x)\mathbf{a} = e^{-i\omega_\mathrm{d} L}\mathbf{a} - t_{\mathrm{BM}}\, e^{-i\omega_\mathrm{d} L/2}\mathbf{A}^{(0)}_{\mathrm{in}} \qquad [22]$$

for the field $\mathbf{a} = (a_{r,n=1,\ldots,N_y}, a_{u,n}, a_{l,n}; a_{d,n})^T$, where $A^{(0)}_{\mathrm{out}}$ is the amplitude of the output field $A^{(0)}_{\mathrm{out},m} = A^{(0)}_{\mathrm{out}} e^{ik_x m - i\omega_\mathrm{d} t}/\sqrt{N_x}$, R_{BM} is obtained by replacing the diagonal matrix element $I_{3N_y+1,3N_y+1}$ of the $4N_y$-dimensional identity matrix I with ir_{BM},

$$S_0(k_x) = \frac{1}{\sqrt{2}} \begin{pmatrix} 0 & ie^{-ik_x} e^{-in\sigma\theta_0} & 0 & e^{-ik_x} e^{-in\sigma\theta_0} \\ i & 0 & 1 & 0 \\ 0 & e^{ik_x} e^{in\sigma\theta_0} & 0 & ie^{ik_x} e^{in\sigma\theta_0} \\ 1 & 0 & i & 0 \end{pmatrix}, \qquad [23]$$

and $\mathbf{A}^{(0)}_{\mathrm{in}} = A^{(0)}_{\mathrm{in}}(\mathbf{0};\mathbf{0};\mathbf{0};\mathbf{1})^T$ is composed of the N_y-dimensional null vector $\mathbf{0}$ and $\mathbf{1} = (1, 0, \ldots, 0)$.

The solution of the scattering Eq. **22** determines the output amplitude

$$A^{(0)}_{\mathrm{out}} = \frac{t_{\mathrm{BM}}}{ir_{\mathrm{BM}}} e^{-i\omega_\mathrm{d} L/2} a_{d,1} - \frac{A^{(0)}_{\mathrm{in}}}{ir_{\mathrm{BM}}}. \qquad [24]$$

When the driving frequency ω_d is resonant with an eigenfrequency of the closed system, the boundary condition **21** gives the amplitude

$$a_{d,1} = \frac{t_{\mathrm{BM}}}{1 - ir_{\mathrm{BM}}} A^{(0)}_{\mathrm{in}}\, e^{i\omega_\mathrm{d} L/2}, \qquad [25]$$

and the input–output relation $A^{(0)}_{\mathrm{out}} = e^{i\delta_0} A^{(0)}_{\mathrm{in}}$, where the phase shift

$$\delta_0 = \arg\left(\frac{1 + ir_{\mathrm{BM}}}{1 - ir_{\mathrm{BM}}}\right). \qquad [26]$$

Remarkably, the relative phase $\delta_0 - (\pi + 2\arctan r_{\mathrm{BM}}) \in (-\pi, \pi]$ jumps from $-\pi$ to π when ω_d sweeps across a resonant frequency of the closed network. Thus, the measurement of this phase shift reveals the spectrum. As shown in Fig. 4*A*, for σ_+ polarized driving light, the peaks of $d\delta_0/d\omega_\mathrm{d}$ show the band structure and the chiral edge mode on the top boundary. The spatial separation of the bottom edge mode and the driving light makes the first invisible in Fig. 4*A*, which isolates a single σ_+ polarized chiral edge mode on the top boundary.

For the planar network, circularly polarized driving light with amplitude $A^{(0)}_{\mathrm{in}}$ and frequency ω_d is injected through the transmissive mirror at the upper left corner (Fig. 1*C*). The boundary condition **16** and the scattering equation

$$\bar{R}_{\mathrm{BM}} S_0 \mathbf{a} = e^{-i\omega_\mathrm{d} L}\mathbf{a} - t_{\mathrm{BM}}\, e^{-i\omega_\mathrm{d} L/2}\mathbf{A}^{(0)}_{\mathrm{in}} \qquad [27]$$

determine the light distribution $\mathbf{a} = (a_{r,nm}, a_{u,nm}, a_{l,nm}, a_{d,nm})^T$ in the open network, where $\bar{R}_{\mathrm{BM}}$ is obtained by replacing the diagonal matrix elements $I_{1,1}$ and $I_{3N_xN_y,3N_xN_y}$ of the $4N_xN_y$-dimensional identity matrix I with ir_{BM}, and $\mathbf{A}^{(0)}_{\mathrm{in}} = A^{(0)}_{\mathrm{in}}(\mathbf{1};\mathbf{0};\mathbf{0};\mathbf{0})^T$.

The solution of the scattering Eq. **27** determines the reflection and transmission amplitudes

$$A_{\mathrm{R}} = \frac{t_{\mathrm{BM}}}{ir_{\mathrm{BM}}} a_{r,11}\, e^{-i\omega_\mathrm{d} L/2} - \frac{A^{(0)}_{\mathrm{in}}}{ir_{\mathrm{BM}}},$$
$$A_{\mathrm{T}} = \frac{t_{\mathrm{BM}}}{ir_{\mathrm{BM}}} a_{l,N_yN_x}\, e^{-i\omega_\mathrm{d} L/2}. \qquad [28]$$

As shown in Fig. 4*B*, the transmission spectrum $|A_{\mathrm{T}}/A^{(0)}_{\mathrm{in}}|^2$ of the output light through the mirror at the bottom right corner

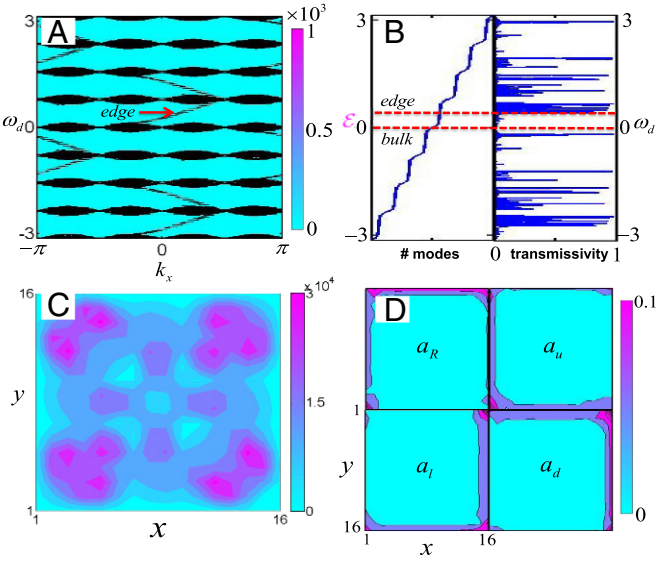

Fig. 4. Detection of topological properties, where $\theta_0 = \pi/2$, $r_{\mathrm{BM}} = 0.9$, and L is taken as a unit. (*A*) For the cylindrical geometry, the contour-plot of $d\delta_0/d\omega_\mathrm{d}$ shows the eigenspectrum for the network of size 48×48. (*B*) For the open plane of size 16×16, the eigenspectrum for the closed network and the transmission spectrum. (*C*) The light intensity of the bulk mode under the σ_+-polarized driving light. (*D*) The light intensities $|a_{(r,\,u,\,l,\,d)}/A^{(0)}_{\mathrm{in}}|^2$ of the edge mode in the network under σ_+-polarized driving light. From the right- (left-) and up- (down-)moving fields shown in the *Top* (*Bottom*) row, the chirality of the edge mode can be identified.

can be identified with the energy spectrum. For a driving frequency $\omega_d \sim 0.03/L$ $(0.37/L)$ resonant with the bulk (edge) mode, as shown in Fig. 4*C* (Fig. 4*D*), the intensities $|a_{(r,u,l,d),nm}/A_{in}^{(0)}|^2$ display that the light propagates in the bulk (along the boundary).

Robustness of the Edge Modes in Open Networks. To analyze the robustness of edge modes, we take into account possible imperfections in the network, including losses and phase fluctuations of the linear elements. The edge modes generated by the external driving field are robust, which is the result of the broad topological bandwidth and bandgap. In *Robustness of Broadband Setups* and Figs. S3 and S4, we construct another topological network with the tunable spectral width and show that a spectrum spreading over the whole FSR has a dramatic effect on the robustness.

To show the differences of our network and that in ref. 15, we use the same input–output configuration, namely, pumping the network through the node $(1,1)$ and detecting the transmission light at the node $(N_y,1)$. The loss of each element is chosen to be 0.1% in the linear optical system. In Fig. 5, the light intensity $I=\sum_{s=r,u,l,d}|a_{s,nm}|^2$ in the steady edge state shows that the edge mode completely circulates around the 16×16 network.

The short lifetime of the edge modes in the narrow-band setup can be overcome in the broadband setup. In the narrow-band setup, each resonator has a high finesse $(\sim 10^2)$, such that the light reflects many times in the resonator, which induces a large decay to undesired modes. In the broadband setup, the low finesse (~ 1) of the resonator results in a short time of the light in the resonator and the small loss to the undesired modes.

Even though the system is not completely immune to the losses and imperfections that break the TR symmetry and induce backscattering that changes the polarization, the imperfections are strongly suppressed due to the broad width of the spectrum. We note that the birefringent element is a linear element, which cannot break the TR symmetry. The TR symmetry breaking mentioned here amounts to the coupling between two polarizations with opposite chiralities.

For instance, small phase fluctuations δ and δ' of birefringent elements, i.e., $X=e^{i\sigma_x(\pi/4+\delta)}$ and $X^\dagger=e^{-i\sigma_x(\pi/4+\delta')}$, can induce the coupling between σ_+ and σ_- polarized light. We consider driving the planar network of size 16×16 through the node $(1,1)$ with σ_+-polarized light and detecting the transmitted light at the node $(16,1)$. In Fig. 6, the intensities of $\sigma_\pm$-polarized edge modes are shown for $\delta,\delta'\in[-0.05,0.05]$ and $\delta,\delta'\in[-0.1,0.1]$. For random phase fluctuations $\delta,\delta'\in[-0.05,0.05]$, 1% σ_+-polarized clockwise propagating light in the network is scattered to σ_--polarized anticlockwise propagating light, and 1% σ_--polarized light is detected in the transmitted light. For the larger phase fluctuations $\delta,\delta'\in[-0.1,0.1]$, 10% σ_+-polarized clockwise propagating light in the network is scattered to σ_--polarized anticlockwise propagating light, and 12% σ_--polarized light is detected in the transmitted light. In real experiments, phase fluctuations of linear optical elements can be much smaller than 0.05. As a result, in the steady state, 99% σ_+-polarized chiral mode may survive at the boundary of the network.

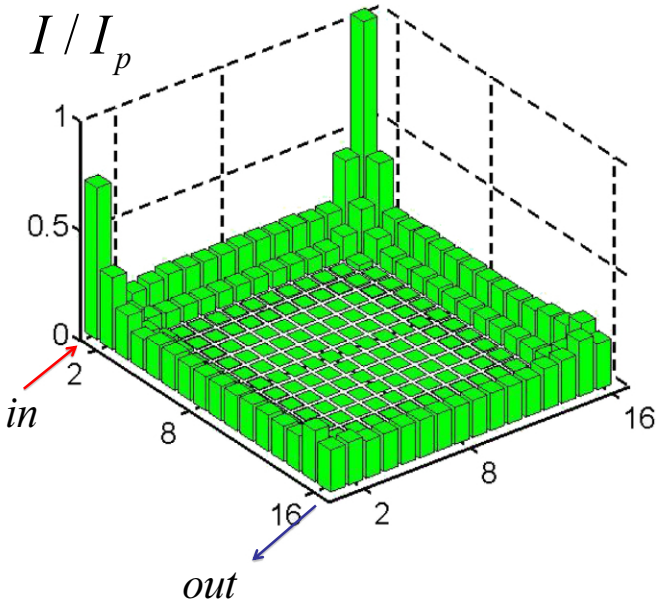

Fig. 5. The intensity of the steady edge mode in the open planar network, where the intrinsic loss is 0.1%, and I_p is the intensity of the pump field.

Nonlinear Regime

In this section, we study how the topological properties predicted in the previous section get modified in the nonlinear regime. We restrict ourselves to the cylindrical network. By driving the open network from the top boundary, we show in *Topological Band Structures in Closed Networks* that bulk and edge steady states are both generated. In *Probe Edge and Bulk Modes in Open Networks*, we analyze the stability of the steady states by means of a generalized Bogoliubov theory, where it turns out that the Bogoliubov edge mode can be detected by the squeezing spectrum of the reflected light.

The nonlinear Kerr medium generates a self-focusing interaction for $\chi<0$. Here, we consider separately the $\sigma_\pm$ polarizations and thereby avoid the complexity associated to a Kerr nonlinearity for $\sigma_\pm$ polarizations propagating simultaneously in the fiber links (43, 44). The relations **8** and **9** give rise to the scattering equation

$$S_0\begin{pmatrix}a_{r,nm}\\ a_{u,nm}\\ a_{l,nm}\\ a_{d,nm}\end{pmatrix}=e^{-i\omega L}e^{i\chi\mathcal{N}_{nm}L}\begin{pmatrix}a_{r,nm+1}\\ a_{u,n-1m}\\ a_{l,nm-1}\\ a_{d,n+1m}\end{pmatrix} \qquad [29]$$

for the bulk degrees of freedom, where the 4×4 intensity-dependent matrix $\mathcal{N}_{nm}$ is defined in *Scattering Equations on Different Geometries*.

The effective Hamiltonian provides an insight into the physics in the interacting case. By projecting the system on a certain band, the effective Hamiltonian can be interpreted as describing weak interacting bosons in a topological band. At the mean-field level, we could expect that the steady state is a Bose–Einstein condensate of light, and the fluctuations are described by Bogoliubov modes that give rise to squeezing. In the following, we focus on the steady state and fluctuations in the cylindrical network.

Steady-State Solutions. To generate the interacting bulk and edge steady states, we consider driving the cylindrical network by an external field. Circularly polarized pump-field $A_{in,m}^{(0)}e^{-i\omega_d t}$ with amplitude $A_{in,m}^{(0)}=A_{in}^{(0)}e^{ik_x m}/\sqrt{N_x}$ is applied through the top boundary. Due to the translational symmetry along the x direction, the steady-state solution of Eq. **29** has the form **19**.

By numerically solving Eq. **29** with the boundary condition **21**, we show the total light intensity $N_p=\sum_{n,s=r,u,l,d}|a_{s,n}|^2$ vs. the driving strength $\left|A_{in}^{(0)}\right|^2$ in Fig. 7 *A* and *B* for two driving frequencies $\omega_d^{(1)}\sim 0.22/L$ (Fig. 7*A*) and $\omega_d^{(2)}\sim 4.5\times 10^{-2}/L$ (Fig. 7*B*), respectively, where $k_x\sim 0.26$ and the size of the network is $N_x=24$, $N_y=12$. The $|\chi|\,N_p$ vs. $|\chi|\left|A_{in}^{(0)}\right|^2$ curves display that for the given parameters (k_x,ω_d), the driving light with amplitude

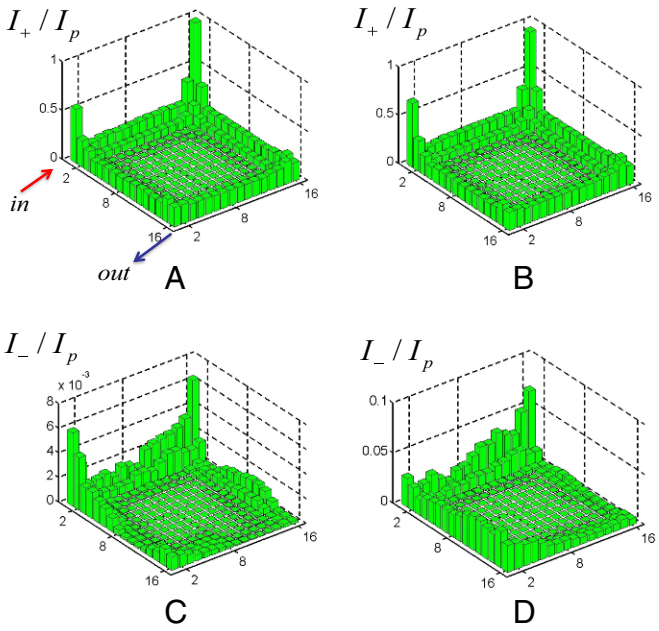

Fig. 6. *A* and *C* show the intensities $I_\pm/I_p$ of the $\sigma_\pm$-polarized light in the network for δ, $\delta' \in [-0.05, 0.05]$; *B* and *D* show the intensities $I_\pm/I_p$ of the $\sigma_\pm$-polarized light in the network for δ, $\delta' \in [-0.1, 0.1]$.

$A_{\rm in}^{(0)}$ generates multiple light intensities in the steady state of the network. As discussed in *Bogoliubov Excitations in Nonlinear Optics*, large domains of the steady-state solutions in Fig. 7 *A* and *B* are unstable to small perturbations. The qualitative origin of these complex stabilities can be traced to the behavior of a single fiber segment with mirrors (47) (*Light Propagation in Single-Segment Nonlinear Fiber* and Fig. S2).

For driving frequencies $\omega_{\rm d}^{(1)}$ and $\omega_{\rm d}^{(2)}$, Fig. 7 *C* and *D* shows that distinct light distributions $|\chi|\left|a_{(r,u,l,d),n}\right|^2$ are generated for the interacting edge and bulk modes, respectively, where the total intensity $|\chi|\, N_{\rm p} = 5/L$, and $r_{\rm BM} = 0.9$. We emphasize that the topologically protected chiral edge mode survives even in the nonlinear regime, as illustrated in Fig. 7*C*, where the chirality can be gathered from the fact that the right-moving intensity dominates.

Bogoliubov Excitations in Nonlinear Optics. The stability of steady-state solutions is analyzed in this subsection. Small fluctuations around the driving field $A_{{\rm in},m}^{(0)}$ induce excitations around the steady state. If excitation is exponentially amplified in the real-time evolution, the steady state is not stable. We develop a generalized Bogoliubov theory to analyze the properties of the fluctuations and the stability of the steady states. We show that around the stable steady state, chiral Bogoliubov edge excitations are squeezed and can be detected by the squeezing spectrum of the reflected light.

The additional weak probe light

$$\delta A_m^{\rm in}(t) = \frac{1}{\sqrt{N_x}}[\delta A_{\rm in}^{(+)} e^{ip_x m} e^{-i\omega_{\rm f} t} + \delta A_{\rm in}^{(-)} e^{iq_x m} e^{i\omega_{\rm f} t}] \quad [30]$$

with frequency $\omega_{\rm f}$ through the top boundary induces the fluctuation field δa_s around the steady-state a_s and the reflected fluctuation field $\delta A_m^{\rm out}(t)$, where p_x and $q_x = 2k_x - p_x$ are the quasi-momenta along the x direction.

To establish the scattering equation for the fluctuation amplitudes δa_s in the entire network, we first study the propagation of fluctuation fields in the fiber. By linearizing the motion in Eqs. **4** and **5**, we obtain

$$i\partial_t \delta\Psi_H + \Sigma\partial_x \delta\Psi_H = \mathbf{M}_H \delta\Psi_H, \quad [31]$$

and

$$i\partial_t \delta\Psi_V + \Sigma\partial_x \delta\Psi_V = \mathbf{M}_V \delta\Psi_V, \quad [32]$$

which describe the dynamics of Bogoliubov fluctuations

$$\delta\Psi_H = (\delta\phi_{r,nm}, \delta\phi_{l,nm-1}, \delta\phi^*_{r,nm}, \delta\phi^*_{l,nm-1})^T,$$
$$\delta\Psi_V = (\delta\phi_{u,nm}, \delta\phi_{d,n+1m}, \delta\phi^*_{u,nm}, \delta\phi^*_{d,n+1m})^T \quad [33]$$

in the horizontal and vertical fibers, respectively. Here, the matrices Σ and $\mathbf{M}_{H(V)}$ are defined in *Light Propagation in Single-Segment Nonlinear Fiber*.

The solution of linearized Eqs. **31** and **32** has the form

$$\delta\phi_{s,nm}(x,t) = \frac{1}{\sqrt{N_x}}[\delta\psi_{s,n,p_x}(x) e^{ip_x m} e^{-i\omega_{\rm f} t} + \delta\psi_{s,n,q_x}(x) e^{iq_x m} e^{i\omega_{\rm f} t}]. \quad [34]$$

The input and output fluctuation fields at the nodes modulate along the x direction with the quasi-momenta p_x and q_x, where the fluctuation amplitudes are related to the boundary value of the wavefunctions ψ_{r,n,p_x} and ψ_{r,n,q_x} as

$$\delta a_{r,n,p_x} = \delta\psi_{r,n,p_x}(L), \delta a_{l,n,p_x} = e^{in\sigma\theta_0}\delta\psi_{l,n,p_x}(0),$$
$$\delta b_{r,n,p_x} = e^{in\sigma\theta_0}\delta\psi_{r,n,p_x}(0), \delta b_{l,n,p_x} = \delta\psi_{l,n,p_x}(L),$$
$$\delta a_{u,n,p_x} = \delta\psi_{u,n,p_x}(L), \delta a_{d,n+1,p_x} = \delta\psi_{d,n+1,p_x}(0),$$
$$\delta b_{u,n,p_x} = \delta\psi_{u,n,p_x}(0), \delta b_{d,n+1,p_x} = \delta\psi_{d,n+1,p_x}(L). \quad [35]$$

The scattering Eqs. **31** and **32** result in the relations

$$\bar{P}_H \begin{pmatrix} e^{-in\sigma\theta_0}\delta b_{r,n,p_x} \\ e^{-in\sigma\theta_0}\delta a_{l,n,p_x} \\ e^{in\sigma\theta_0}\delta b^*_{r,n,q_x} \\ e^{in\sigma\theta_0}\delta a^*_{l,n,q_x} \end{pmatrix} = \begin{pmatrix} \delta a_{r,n,p_x} \\ \delta b_{l,n,p_x} \\ \delta a^*_{r,n,q_x} \\ \delta b^*_{l,n,q_x} \end{pmatrix}, \quad [36]$$

and

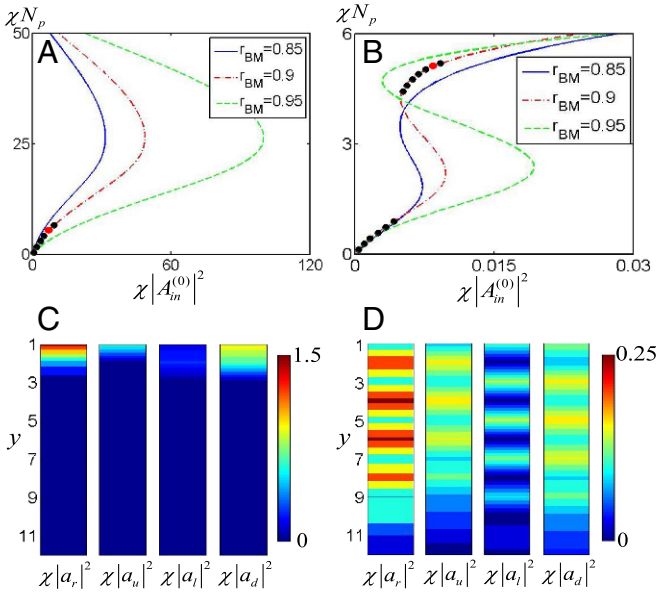

Fig. 7. Light distributions of the nonlinear system in the cylinder, where the size is 24 × 12, $\theta_0 = \pi/2$, $k_x = 0.26$, and L is taken as a unit. (*A* and *B*) The relation of the total intensity of (*A*) edge and (*B*) bulk modes in the network with different reflection indexes $r_{\rm BM}$ and the input intensity of driving light with frequencies (*A*) $\omega_{\rm d}^{(1)} = 0.22$ and (*B*) $\omega_{\rm d}^{(2)} = 4.5 \times 10^{-2}$. (*C* and *D*) The stable internal intensities of (*C*) edge and (*D*) bulk modes for $|\chi|\, N_{\rm p} = 5$ and $r_{\rm BM} = 0.9$ (red circles in *A* and *B*).

$$\bar{P}_V \begin{pmatrix} \delta b_{u,n,p_x} \\ \delta a_{d,n+1,p_x} \\ \delta b^*_{u,n,q_x} \\ \delta a^*_{d,n+1,q_x} \end{pmatrix} = \begin{pmatrix} \delta a_{u,n,p_x} \\ \delta b_{d,n+1,p_x} \\ \delta a^*_{u,n,q_x} \\ \delta b^*_{d,n+1,q_x} \end{pmatrix} \quad [37]$$

connecting the boundary values of the fields in the horizontal and vertical fibers, respectively, where the propagation matrices $\bar{P}_{H(V)} = e^{\Sigma(\omega_f - \tilde{\mathbf{M}}_{H(V)})L}$ and $\tilde{\mathbf{M}}_{H(V)}$ are defined in *Propagation Matrices of Bogoliubov Excitations*.

Additionally, the boundary values of the fields in adjacent fibers are related by the input–output formula

$$S_{f,\mathrm{node}}(p_x) \begin{pmatrix} \delta a_{r,n,p_x} \\ \delta a_{u,n,p_x} \\ \delta a_{l,n,p_x} \\ \delta a_{d,n,p_x} \end{pmatrix} = \begin{pmatrix} e^{ip_x}\delta b_{r,n,p_x} \\ \delta b_{u,n-1,p_x} \\ e^{-ip_x}\delta b_{l,n,p_x} \\ \delta b_{d,n+1,p_x} \end{pmatrix} \quad [38]$$

at each node, where

$$S_{f,\mathrm{node}}(p_x) = e^{i\omega_d L} e^{-i\frac{\chi}{N_x}\mathcal{N}_n L} \begin{pmatrix} e^{-ip_x} & 0 & 0 & 0 \\ 0 & 1 & 0 & 0 \\ 0 & 0 & e^{ip_x} & 0 \\ 0 & 0 & 0 & 1 \end{pmatrix} S_{\mathrm{node}}. \quad [39]$$

The propagation Eqs. **36** and **37** and the input–output relation **38** result in the scattering equation for the fluctuation amplitudes in the bulk. To analyze the properties of those fluctuations and the stability of the steady states, the boundary conditions for the fluctuation fields are required.

The boundary condition

$$\begin{aligned} ir_{\mathrm{BM}}\delta b_{u,0,p_x} &= e^{-i\omega_f L}\delta a_{d,1,p_x} - t_{\mathrm{BM}}\delta A^{(+)}_{\mathrm{in}} e^{i(\omega_d-\omega_f)\frac{L}{2}}, \\ ir_{\mathrm{BM}}\delta b_{u,0,q_x} &= e^{i\omega_f L}\delta a_{d,1,q_x} - t_{\mathrm{BM}}\delta A^{(-)}_{\mathrm{in}} e^{i(\omega_d+\omega_f)\frac{L}{2}}, \end{aligned} \quad [40]$$

for the fluctuation amplitudes follows from Eq. **21**, and the output field is

$$\delta A^{\mathrm{out}}_m(t) = \frac{1}{\sqrt{N_x}}[\delta A^{(+)}_{\mathrm{out}} e^{ip_x m} e^{-i\omega_f t} + \delta A^{(-)}_{\mathrm{out}} e^{iq_x m} e^{i\omega_f t}], \quad [41]$$

where the components

$$\begin{aligned} \delta A^{(+)}_{\mathrm{out}} &= \frac{t_{\mathrm{BM}}}{ir_{\mathrm{BM}}} e^{-i(\omega_d+\omega_f)\frac{L}{2}}\delta a_{d,1,p_x} - \frac{\delta A^{(+)}_{\mathrm{in}}}{ir_{\mathrm{BM}}}, \\ \delta A^{(-)}_{\mathrm{out}} &= \frac{t_{\mathrm{BM}}}{ir_{\mathrm{BM}}} e^{-i(\omega_d-\omega_f)\frac{L}{2}}\delta a_{d,1,q_x} - \frac{\delta A^{(-)}_{\mathrm{in}}}{ir_{\mathrm{BM}}}. \end{aligned} \quad [42]$$

Eliminating the output fluctuation fields $\delta b_{s,n,p_x(q_x)}$ in Eqs. **36**–**38** and **40**, we establish the linearized scattering equation

$$\mathbf{D}(\omega_f) \begin{pmatrix} \delta \mathbf{a}_{p_x} \\ \delta \mathbf{a}^*_{q_x} \end{pmatrix} = t_{\mathrm{BM}} \begin{pmatrix} \delta \mathbf{A}^{(+)}_{\mathrm{in}} e^{i(\omega_d-\omega_f)\frac{L}{2}} \\ \delta \mathbf{A}^{(-)*}_{\mathrm{in}} e^{-i(\omega_d+\omega_f)\frac{L}{2}} \end{pmatrix} \quad [43]$$

for the fluctuations, where

$$\delta \mathbf{a}_{p_x} = (\delta a_{r,n,p_x}, \delta a_{u,n,p_x}, \delta a_{l,n,p_x}, \delta a_{d,n,p_x})^T, \quad [44]$$

and $\delta \mathbf{A}^{(\pm)}_{\mathrm{in}} = \delta A^{(\pm)}_{\mathrm{in}}(\mathbf{0};\mathbf{0};\mathbf{0};\mathbf{1})$. The steady state is stable if the fluctuations are not amplified during the time evolution. This stable condition demands that all of the roots $\mathcal{E}_f$ of $\det\mathbf{D}(\omega_f)$ have negative imaginary part, i.e., $\mathrm{Im}\mathcal{E}_f < 0$.

By solving the fluctuation Eq. **43**, we mark the stable regimes by black circles in the χN_p vs. $\chi\left|A^{(0)}_{\mathrm{in}}\right|^2$ curves for the steady states with $r_{\mathrm{BM}} = 0.9$ in Fig. 7 *A* and *B*. We find that the steady states shown in Fig. 7 *C* and *D* are in the stable regime.

Eq. **42** and the solution $(\delta \mathbf{a}_{p_x}, \delta \mathbf{a}^*_{q_x})$ of Eq. **43** lead to the input–output relation

$$\begin{pmatrix} \delta A^{(+)}_{\mathrm{out}} \\ \delta A^{(-)*}_{\mathrm{out}} \end{pmatrix} = M_{\mathrm{IO}} \begin{pmatrix} \delta A^{(+)}_{\mathrm{in}} \\ \delta A^{(-)*}_{\mathrm{in}} \end{pmatrix}, \quad [45]$$

where the 2×2 matrix

$$M_{\mathrm{IO}} = \frac{1}{ir_{\mathrm{BM}}}\sigma_z[t^2_{\mathrm{BM}} e^{-i\omega_f L} e^{-i\omega_d \frac{L}{2}\sigma_z} \tilde{D}(\omega) e^{i\omega_d \frac{L}{2}\sigma_z} - I_2] \quad [46]$$

is determined by

$$\tilde{D}(\omega) = \begin{pmatrix} [\mathbf{D}^{-1}(\omega)]_{3N_y+1,3N_y+1} & [\mathbf{D}^{-1}(\omega)]_{3N_y+1,7N_y+1} \\ [\mathbf{D}^{-1}(\omega)]_{7N_y+1,3N_y+1} & [\mathbf{D}^{-1}(\omega)]_{7N_y+1,7N_y+1} \end{pmatrix}. \quad [47]$$

Induced by the light "condensation" $a_{s,n}$, the Bogoliubov fluctuation $\delta a_{s,p_x,n}$ couples to the conjugate amplitude $\delta a^*_{s,q_x,n}$. As a result, the probe light with positive frequency, i.e., $\delta A^{(-)}_{\mathrm{in}} = 0$, induces a chiral Bogoliubov fluctuation, which eventually generates the squeezed reflected light $\delta A_{\mathrm{out},m}(t)$. (We emphasize that our results from the fluctuation analysis for the classical light are also valid in the quantum regime, where the squeezing behaviors of quantum edge fluctuations arise from the interplay of the Kerr nonlinearities and topological effects.) The squeezing behavior is characterized by the squeezing spectra $S_+ = \left|\delta A^{(+)}_{\mathrm{out}}/\delta A^{(+)}_{\mathrm{in}}\right|$ and $S_- = \left|\delta A^{(-)}_{\mathrm{out}}/\delta A^{(+)}_{\mathrm{in}}\right|$, where the expression $S^2_+ - S^2_- = 1$ reflects the bosonic nature of light.

We note that squeezing of light in topological insulators has been investigated in the context of optical parametric down-conversion systems (24), where the $\chi^{(2)}$ nonlinearity is treated at the mean-field level and quadratic terms with double creation (annihilation) operators are directly introduced in the Hamiltonian to describe the generation of squeezed light.

Around the stable edge steady state (Fig. 7*C*), the probe field with momentum $p_x \sim 0.52$ induces the generation of squeezed light with the spectra displayed in Fig. 8*A*. Here, we chose this quasi-momentum, because the edge mode is more isolated from the bulk modes and has the smallest localization length. The peak around the frequency $\omega_f \sim 0.35/L$ in the squeezing spectra is the signature of chiral Bogoliubov fluctuations $\delta \mathbf{a}_{p_x}$ and $\delta \mathbf{a}^*_{q_x}$. As shown in Fig. 8*B*, the large light distribution at the top boundary generates a strong coupling of Bogoliubov fluctuations localized at the edge, which results in comparable magnitudes of $\delta \mathbf{a}_{p_x}$ and $\delta \mathbf{a}^*_{q_x}$. In the bulk steady state (Fig. 7*D*), edge fluctuations can also be generated by a probe light. However, due to the small light distribution along the boundary, the counterpart $\left|\delta \mathbf{a}^*_{q_x}/\delta A^{(+)}_{\mathrm{in}}\right| \sim 10^{-3}$ and thus the

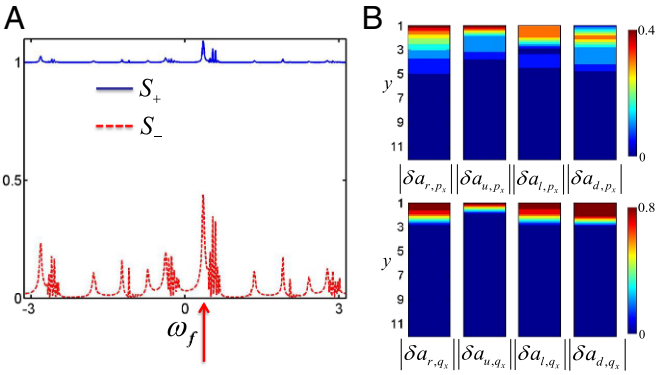

Fig. 8. Bogoliubov fluctuations in the cylinder, where the system size is 24×12, $\theta_0 = \pi/2$. The amplitude $|\delta A^{(+)}_{\mathrm{in}}|$ of the probe light and L are taken as a unit. (*A*) The squeezing spectra of the probe field with the positive frequency, where the Bogoliubov fluctuations above the stable edge steady states are generated. (*B*) The distributions of Bogoliubov edge fluctuations above the stable edge steady states, where the Bogoliubov excitation has the frequency $\omega_f = 0.35$, shown by the red arrow in *A*.

edge Bogoliubov fluctuations hardly respond to the driving field $\delta A_{\rm in}^{(+)}$.

In this nonlinear regime our system displays a set of phenomena that are quite different from the results in previous works (51–55): (*i*) A closed nonlinear network is unstable, and the system becomes stable by including losses; (*ii*) around the stable edge steady state, a probe field with a second frequency develops small edge Bogoliubov fluctuations which turn out to be chiral; (*iii*) the presence of squeezing, a quantum feature, is identified in the edge modes. The reason for the appearance of these phenomena is that the energy bands in different FSRs connect to each other, so that the system cannot be described by a lower-bounded Hamiltonian.

Experimental Parameters

In experimental implementations, one could take a fiber with $L = 50$ μm and cross section 2×10^{-7} cm^2, such that the bands spread over the broad FSR with 1 THz in the linear network.

For the nonlinear network, the relevant parameter is the unitless phase $\varphi = \chi \left| A_{\rm in}^{(0)} \right|^2 L$ induced by the Kerr interaction. In terms of the experimental parameters, the phase $\varphi \sim 2 k_0 n_2 I_0 L$ is determined by the wavevector k_0 in the optical fiber, the second-order nonlinear refractive index n_2, the intensity $I_0 = P/A$ (power/area) of the pump field, and the length of the fiber L, where the optical fiber with $k_0 \sim 4.2 \times 10^4$ cm^{-1}, and the section $A \sim 2 \times 10^{-7}$ cm^2.

For the electronic Kerr effect with small $n_2 \sim 10^{-16}$ cm^2/W, a length of the link $L \sim 10$ m of the fiber and a power $P = 20$ W of the pump field should be large enough to realize a phase shift $\varphi \sim 1$. To realize the large nonlinearity in the small network with $L \sim 50$ μm, one can use the thermal Kerr effect with $n_2 \sim 10^{-6}$ cm$^2/W$. A pump power P_0 ranging from 4×10^{-4} W to 4×10^{-3} W gives rise to nonlinear phase shifts ranging from $\varphi = 1 \sim 10$.

We note that our proposal could also be implemented in the all-in-fiber temporal lattice setup (56).

Conclusions

We have proposed a scheme to display QSH phenomena using classical light and passive optical elements. Compared with previous schemes, ours features broad topological bandgaps. For open networks in the linear regime, chiral edge modes appear at the bandgaps and are very robust against losses and random phase fluctuations. Adding Kerr nonlinearities in the fibers leads to interacting bulk and edge states that also display topological properties. For closed networks, the system becomes unstable. This can be avoided by opening it. We also predict squeezing in the chiral edge modes.

ACKNOWLEDGMENTS. This work was funded by the European Union Integrated project SIQS. H.J.K. acknowledges support as a Max-Planck Institute for Quantum Optics Distinguished Scholar; as well as funding from the Air Force Office of Scientific Research Multidisciplinary University Research Initiative (MURI) Quantum Many-Body Physics with Photons; the Office of Naval Research (ONR) Award N00014-16-1-2399; the ONR Quantum Opto-Mechanics with Atoms and Nanostructured Diamond (QOMAND) MURI; National Science Foundation (NSF) Grant PHY-1205729; and the Institute for Quantum Information and Matter, an NSF Physics Frontiers Center.

1. Thouless DJ, Kohmoto M, Nightingale MP, den Nijs M (1982) Quantized Hall conductance in a two-dimensional periodic potential. *Phys Rev Lett* 49:405–408.
2. Haldane FDM (1988) Model for a quantum Hall effect without Landau levels: Condensed-matter realization of the "parity anomaly". *Phys Rev Lett* 61:2015–2018.
3. Hasan MZ, Kane CL (2010) Colloquium: Topological insulators. *Rev Mod Phys* 82:3045–3067.
4. Qi X-L, Zhang S-C (2011) Topological insulators and superconductors. *Rev Mod Phys* 83:1057–1110.
5. Kane CL, Mele EJ (2005) Quantum spin Hall effect in graphene. *Phys Rev Lett* 95:226801.
6. König M, et al. (2007) Quantum spin Hall insulator state in HgTe quantum wells. *Science* 318:766–770.
7. Hsieh D, et al. (2008) A topological Dirac insulator in a quantum spin Hall phase. *Nature* 452:970–974.
8. Zhang H, et al. (2009) Topological insulators in Bi2Se3, Bi2Te3 and Sb2Te3 with a single Dirac cone on the surface. *Nat Phys* 5:438–442.
9. Chang CZ, et al. (2013) Experimental observation of the quantum anomalous Hall effect in a magnetic topological insulator. *Science* 340:167–170.
10. Kane CL, Mele EJ (2005) Z_2 topological order and the quantum spin Hall effect. *Phys Rev Lett* 95:146802.
11. Fu L, Kane CL (2006) Time reversal polarization and a Z_2 adiabatic spin pump. *Phys Rev B* 74:195312.
12. Wen XG (1992) Theory of the edge states in fractional quantum Hall effects. *Int J Mod Phys B* 6:1711–1762.
13. Laughlin RB (1983) Anomalous quantum Hall effect: An incompressible quantum fluid with fractionally charged excitations. *Phys Rev Lett* 50:1395–1398.
14. Moore G, Read N (1991) Nonabelions in the fractional quantum Hall effect. *Nucl Phys B* 360:362–396.
15. Hafezi M, Mittal S, Fan J, Migdall A, Taylor JM (2013) Imaging topological edge states in silicon photonics. *Nat Photon* 7:1001–1005.
16. Rechtsman MC, et al. (2013) Photonic Floquet topological insulators. *Nature* 496:196–200.
17. Dalibard J, Gerbier J, Juzeliūnas F, Öhberg G (2011) Colloquium: Artificial gauge potentials for neutral atoms. *Rev Mod Phys* 83:1523–1543.
18. Shi T, Cirac JI (2013) Topological phenomena in trapped-ion systems. *Phys Rev A* 87:013606.
19. Haldane FDM, Raghu S (2008) Possible realization of directional optical waveguides in photonic crystals with broken time-reversal symmetry. *Phys Rev Lett* 100:013904.
20. Wang Z, Chong Y, Joannopoulos JD, Soljačić M (2009) Observation of unidirectional backscattering-immune topological electromagnetic states. *Nature* 461:772–775.
21. Fang K, Yu Z, Fan S (2012) Realizing effective magnetic field for photons by controlling the phase of dynamic modulation. *Nat Photon* 6:782–787.
22. Yuan L, Fan S (2015) Topologically nontrivial Floquet band structure in a system undergoing photonic transitions in the ultrastrong-coupling regime. *Phys Rev A* 92:053822.
23. Walter S, Marquardt F (2016) Classical dynamical gauge fields in optomechanics. *New J Phys* 18:113029.
24. Peano V, Houde M, Brendel C, Marquardt F, Clerk AA (2016) Topological phase transitions and chiral inelastic transport induced by the squeezing of light. *Nat Commun* 7:10779.
25. Umucalılar RO, Carusotto I (2012) Fractional quantum Hall states of photons in an array of dissipative coupled cavities. *Phys Rev Lett* 108:206809.
26. Hafezi M, Demler EA, Lukin MD, Taylor JM (2011) Robust optical delay lines with topological protection. *Nat Phys* 7:907–912.
27. Umucalılar RO, Carusotto I (2011) Artificial gauge field for photons in coupled cavity arrays. *Phys Rev A* 84:043804.
28. Khanikaev AB, et al. (2013) Photonic topological insulators. *Nat Mater* 12:233–239.
29. Pasek M, Chong Y (2014) Network models of photonic Floquet topological insulators. *Phys Rev B* 89:075113.
30. Hu W, et al. (2015) Measurement of a topological edge invariant in a microwave network. *Phys Rev X* 5:011012.
31. Gao F, et al. (2016) Probing topological protection using a designer surface plasmon structure. *Nat Commun* 7:11619.
32. Pendry JB, Holden AJ, Stewart WJ, Youngs I (1996) Extremely low frequency plasmons in metallic mesostructures. *Phys Rev Lett* 76:4773–4776.
33. Smith DR, Padilla WJ, Vier DC, Nemat-Nasser SC, Schultz S (2000) Composite medium with simultaneously negative permeability and permittivity. *Phys Rev Lett* 84:4184–4187.
34. Cheng X, et al. (2016) Robust reconfigurable electromagnetic pathways within a photonic topological insulator. *Nat Mater* 15:542–548.
35. Bahat-Treidel O, Segev M (2011) Nonlinear wave dynamics in honeycomb lattices. *Phys Rev A* 84:021802(R).
36. Bekenstein R, Nemirovsky J, Kaminer I, Segev M (2014) Shape-preserving accelerating electromagnetic wave packets in curved space. *Phys Rev X* 4:011038.
37. Lumer Y, Rechtsman MC, Plotnik Y, Segev M (2016) Instability of bosonic topological edge states in the presence of interactions. *Phys Rev A* 94: 021801(R).
38. Ablowitz MJ, Curtis CW, Ma Y-P (2014) Linear and nonlinear traveling edge waves in optical honeycomb lattices. *Phys Rev A* 90:023813.
39. Leykam D, Chong Y (2016) Edge solitons in nonlinear-photonic topological insulators. *Phys Rev Lett* 117:143901.
40. Rechtsman MC, et al. (2016) Topological protection of photonic path entanglement. *Optica* 3:925–930.
41. Mittal S, Orre VV, Hafezi M (2016) Topologically robust transport of entangled photons in a 2D photonic system. *Opt Express* 24:15631–15641.
42. Bardyn C-E, Karzig T, Refael G, Liew TC (2016) Chiral Bogoliubov excitations in nonlinear bosonic systems. *Phys Rev B* 93:020502(R).
43. Agrawal GP (2013) *Nonlinear Fiber Optics* (Academic, San Diego).
44. Boyd RW (2008) *Nonlinear Optics* (Academic, Rochester, NY).
45. Yu M, McKinstrie CJ, Agrawal GP (1998) Temporal modulation instabilities of counterpropagating waves in a finite dispersive Kerr medium. I. Theoretical model and analysis. *J Opt Soc Am B* 15:607–616.

46. Yu M, McKinstrie CJ, Agrawal GP (1998) Temporal modulation instabilities of counter-propagating waves in a finite dispersive Kerr medium. II. Application to Fabry Perot cavities. *J Opt Soc Am B* 15:617–624.
47. Firth WJ (1981) Stability of nonlinear Fabry-Perot resonators. *Opt Commun* 39:343–346.
48. Adair R, Chase LL, Payne SA (1989) Nonlinear refractive index of optical crystals. *Phys Rev B* 39:3337–3350.
49. Hofstadter DR (1976) Energy levels and wave functions of Bloch electrons in rational and irrational magnetic fields. *Phys Rev B* 14:2239–2249.
50. Rudner MS, Lindner NH, Berg E, Levin M (2013) Anomalous edge states and the bulk-edge correspondence for periodically driven two-dimensional systems. *Phys Rev X* 3:031005.
51. Carusotto I, Ciuti C (2013) Quantum fluids of light. *Rev Mod Phys* 85:299–366.
52. Bleu O, Solnyshkov DD, Malpuech G (2016) Interacting quantum fluid in a polariton chern insulator. *Phys Rev B* 93:085438.
53. Umucalılar RO, Carusotto I (2012) Fractional quantum Hall states of photons in an array of dissipative coupled cavities. *Phys Rev Lett* 108:206809.
54. Lumer Y, Plotnik Y, Rechtsman MC, Segev M (2013) Self-localized states in photonic topological insulators. *Phys Rev Lett* 111:243905.
55. Barnett R (2013) Edge-state instabilities of bosons in a topological band. *Phys Rev A* 88:063631.
56. Regensburger A, et al. (2012) Parity time synthetic photonic lattices. *Nature* 488: 167–171.